Automated analysis of *Physarum* network structure and dynamics

Mark D Fricker[1], Dai Akita[2], Luke LM Heaton[1,3], Nick Jones[3], Boguslaw Obara[4] and Toshiyuki Nakagaki[5]

[1]*Department of Plant Science, University of Oxford, Oxford, OX1 3RB, UK*
[2]*Graduate School of Life Science, Hokkaido University, N10 W8, Sapporo 060-0810, Japan*
[3]*Department of Mathematics, Imperial College, London, SW7 2AZ, UK*
[4]*School of Engineering and Computing Sciences, Durham University, Durham, DH1 3LE, UK*
[5]*Mathematical and Physical Ethology Laboratory,*
Research Center of Mathematics for Social Creativity, Research Institute for Electronic Science,
Hokkaido University, N20 W10, Sapporo 0010020, Japan
(Dated: March 9, 2017)

We evaluate different ridge-enhancement and segmentation methods to automatically extract the network architecture from time-series of *Physarum* plasmodia withdrawing from an arena via a single exit. Whilst all methods gave reasonable results, judged by precision-recall analysis against a ground-truth skeleton, the mean phase angle (Feature Type) from intensity-independent, phase-congruency edge enhancement and watershed segmentation was the most robust to variation in threshold parameters. The resultant single pixel-wide segmented skeleton was converted to a graph representation as a set of weighted adjacency matrices containing the physical dimensions of each vein, and the inter-vein regions. We encapsulate the complete image processing and network analysis pipeline in a downloadable software package, and provide an extensive set of metrics that characterise the network structure, including hierarchical loop decomposition to analyse the nested structure of the developing network. In addition, the change in volume for each vein and intervening plasmodial sheet was used to predict the net flow across the network. The scaling relationships between predicted current, speed and shear force with vein radius were consistent with predictions from Murray's Law. This work was presented at PhysNet 2015

I. INTRODUCTION

Plasmodial slime molds (myxomycetes), such as *Physarum*, and mycelial fungi form elaborate interconnected networks that are highly responsive to local environmental conditions [22]. These networks explore space in the search for food, which is patchily distributed in the environment, and usually present only transiently. As a result, the growing network faces conflicting demands to maximise the search area, whilst minimising the cost of transport and the cost of making the network. Adverse environmental conditions and competition from other organisms also impact the growth and survival of the organism, and the network is continually at risk from damage, predation or disease. Thus, these organisms have evolved in environments where they must achieve efficient compromises between cost, efficiency, and resilience, and studying the adaptive growth of such networks may yield useful insights into the design of de-localized, robust infrastructure networks in other domains [22]. *Physarum* is particularly attractive as a model organism as it is easy to culture, forms a network rapidly within hours that can be readily imaged, and which can be exposed to multiple different treatments in replicate experiments. Thus it is possible to build up a statistical basis to test principles of network self-organisation including problem solving [41, 50, 51], flow optimisation [33], memory [42, 44], or decision making [7, 43].

To make full use of *Physarum* as a model system, it would be advantageous to develop robust, high-throughput methods to extract the complete network architecture and dynamics, to allow comparison between treatments and species, and to provide empirical data to support quantitative modelling. Various groups have developed methods to characterize the biological networks formed by fungi and slime molds [3, 5, 12, 25, 39], and efficient implementations are available to download that work well for well-defined networks (see for example[12, 32]). The simplest method to identify the veins automatically is intensity-based segmentation of a bright-field transmission image to give a binary image, with ones representing the vein structure and zeros for the background. Typically this is followed by thinning of the binary image to give a single-pixel wide skeleton [25]. However, the initial segmentation is critically dependent on the value for the threshold used, and it is rare that a single threshold provides adequate segmentation without either losing thinner, dimmer venules if it is set too high, or artificially expanding and fusing adjacent regions if it is set too low [3, 12]. This is particularly problematic in developing networks of *Physarum* as the veins vary in size and absorbance over an order of magnitude, and the interstitial areas between the veins also contain plasmodial sheet-like regions that are biologically significant, but not normally included as part of the network, as the segmentation algorithms fail in these regions [25]. Local contrast enhancement, adaptive or hysteresis thresholding may improve the initial segmentation [12, 13]. However, these approaches do not

deal well with developmental time-series which contain a range of vein diameters, growing margins and intervening plasmodial sheets. Here we explore additional ridge enhancement methods applied over a range of scales and orientations to selectively highlight curvi-linear features, such as veins within the network structure, prior to segmentation [32, 39].

The skeletonisation process is also problematic as traditional skeletonisation over-segments the binary image and introduces many additional spurs depending on the roughness of the binary outline, which then require pruning [12, 13]. Thinning algorithms perform better, and yield skeletons that match the centreline of the network if the original binary image is symmetrical. Alternatively, watershed algorithms [39], or local fitting to the ridge normal [49], map the centreline directly. In some cases, errors in the segmentation steps can be repaired by post-segmentation correction of the pixel skeleton to fill in gaps [5] or exploit over-segmentation and pruning to capture even fine parts of the network [39].

Once the skeleton has been extracted, it can be used as a template to interrogate the image locally to provide an estimate of the width of the veins. If the original binary image correctly covers the complete vein width, the Euclidean Distance Map (EDM, [25]) or the segmented area-to-length ratio [4], can be used to estimate the width. Alternatively, the original intensity image can be interrogated directly using calibrated measurements of light transmission following the Lambert-Beer law [1], or using greyscale granulometry techniques [39].

Typically, the pixel-skeleton is converted to a graph representation with nodes at the junctions, free ends, and food sources, if present, and the graph edges weighted by their Euclidean length and width [3, 5, 25, 39]. The performance of the segmentation can be estimated visually [3], by comparison with a gold-standard network traced manually [39], or by graph matching following graph conversion [12].

A wide range of network metrics can be calculated from the topological or fully-weighted graph representation [5], or the weighted network can be analysed in terms of fluid flow to estimate transport efficiency [2, 23, 24]. By contrast, there is no single standard measure to evaluate network resilience, as the extent of disruption depends on the type of damage inflicted. Nevertheless, robustness can be evaluated following removal of single edges [51], or as a function of successive edge removal in an ordered or random sequence [6, 8, 17].

In addition to analysis of the network structure itself, the morphology of polygonal regions enclosed by the veins can be analysed to understand the space-filling properties of the network. A dual-graph can be constructed that links each polygonal area to its neighbours, with the strength of the edge determined by the width of the intervening vein. By removing edges in the dual graph in order of their weight and fusing the adjacent areas, the original loopy network can be converted to a binary branching tree, enabling the application of metrics designed for branching trees [26, 36].

This remainder of this paper is structured as follows: Section II reviews the main approaches to ridge enhancement developed originally for segmentation of blood vessels [15], neurons [34], fungal networks [12, 32, 39], or road networks [49]. In Section III, we describe a complete workflow for network extraction and graph conversion using these methods, including a full software implementation. In Section IV, we compare the performance of the different algorithms against a manually-defined ground truth, and demonstrate that all can yield acceptable results if parameter values are tuned carefully. Specifically using the mean phase angle ('Feature Type') from the intensity-independent phase congruency enhancement and watershed segmentation, we analyse the *Physarum* network structure and calculate net flows for networks evacuating a set of enclosed arenas with different geometry. We confirm that flow analysis through the complete network is consistent with predictions of Murray's law [38]. In Section V, we compare the results for analysis of evacuation networks with growing or excision networks.

II. APPROACHES TO RIDGE ENHANCEMENT AND SEGMENTATION

One of the first methods to identify ridges exploited the local curvature of the intensity landscape as estimated from the Hessian (H_σ), comprising second-order partial derivatives, D_{aa} along direction a, of the intensity image (I), where the value of the standard deviation of the Gaussian kernel (σ) is varied over a range of scales that span the sizes of the underlying features [15]:

$$H_\sigma = \begin{bmatrix} D_{xx} & D_{xy} \\ D_{xy} & D_{yy} \end{bmatrix} = \begin{bmatrix} \frac{\delta^2 I}{\delta x^2} * G_\sigma & \frac{\delta^2 I}{\delta x \delta y} * G_\sigma \\ \frac{\delta^2 I}{\delta x \delta y} * G_\sigma & \frac{\delta^2 I}{\delta y^2} * G_\sigma \end{bmatrix} \quad (1)$$

where

$$G_\sigma = \frac{1}{2\pi\sigma^2} e^{-\frac{(x^2+y^2)}{2\sigma^2}} \quad (2)$$

In the resultant scale-space representation, further information on ridge-like features can be extracted from the eigenvalues and eigenvectors of the Hessian, which show characteristic behaviour for a filamentous structure. By ordering the eigenvalues in terms of their absolute magnitude ($|\lambda_1| < |\lambda_2|$, for a 2D image), the smallest eigenvalue ($|\lambda_1|$) denotes the minimum change in intensity, with the corresponding eigenvector oriented along the centreline of the ridge, whilst the largest eigenvalue ($|\lambda_2|$) and eigenvector determine the orientation of the maximum curvature, normal to the ridge centreline. Prominent structures are distinguished from the background by relatively large values of the eigenvalues ($\sqrt{\lambda_1^2 + \lambda_2^2}$). In addition, the ratio $|\lambda_1|/|\lambda_2|$ gives an indication of how blob-like ($|\lambda_1| \approx |\lambda_2|$) or elongated and filament-like ($|\lambda_1| \ll |\lambda_2|$)

the structure is at that point. Thus the 'Vesselness' (V_σ) measure [15], defined by Equation (3), is large at those pixels that are part of a linear structure of scale (σ).

$$V_\sigma = e^{-\frac{\lambda_1^2}{2\beta^2\lambda_2^2}}\left(1 - e^{\frac{\lambda_1^2+\lambda_2^2}{2c^2}}\right) \qquad (3)$$

Note that the relative contributions of the geometric ratio and the intensity components at a given scale (σ) are controlled by the coefficients β and c, respectively. Typically, β is set to 0.5 and c is set to half the maximum Hessian norm. Multi-scale 'Vesselness', for a given set of scales spanning the expected width of the vessels, can be computed as the maximum of the 'Vesselness' values calculated at each scale, and the eigenvectors at that scale used to define local orientation [15].

An alternative weighting of the eigenvalues of the Hessian matrix was proposed by Meijering *et al.* [34]:

$$H' = \begin{bmatrix} D_{xx} + \alpha D_{yy} & (1-\alpha)D_{xy} \\ (1-\alpha)D_{xy} & D_{yy} + \alpha D_{xx} \end{bmatrix} \qquad (4)$$

Where α is set to be $-1/3$ such that the equivalent steerable filter [16] used in the calculation of the Hessian matrix is maximally flat in its longitudinal direction, effectively generating an anisotropic second order Gaussian filter. Conveniently, these kernels can be implemented as steerable filters constructed from a set of basis kernels [16]. The 'Neuriteness' measure at scale σ, (N_σ) is determined from the modified eigenvalues as:

$$N_\sigma = \begin{cases} \frac{\lambda_\sigma}{\lambda_{\sigma,min}} & \text{if } \lambda_\sigma < 0 \\ 0 & \text{if } \lambda_\sigma \geq 0 \end{cases} \qquad (5)$$

where λ_σ is the larger in absolute magnitude of the two modified eigenvalues, and $\lambda_{\sigma,min}$ is the smallest value of λ over all pixels such that:

$$\lambda_{\sigma,1}' = \lambda_{\sigma,1} + \alpha\lambda_{\sigma,2} \qquad (6)$$
$$\lambda_{\sigma,2}' = \lambda_{\sigma,2} + \alpha\lambda_{\sigma,1} \qquad (7)$$
$$\lambda_\sigma = \max\left(|\lambda_{\sigma,1}'|, |\lambda_{\sigma,2}'|\right) \qquad (8)$$
$$\lambda_{\sigma,min} = \min_{\mathbf{p}\in I}(\lambda_\sigma) \qquad (9)$$

$\lambda_{\sigma,1}, \lambda_{\sigma,2}$ are the eigenvalues of the Hessian matrix $H_\sigma(\mathbf{p})$, at pixel $\mathbf{p}$, for a given scale parameter σ.

The use of second-order derivatives of anisotropic Gaussian kernels (SOAGKs) was developed further by Shui *et al.* [47] to improve detection of ridge like elements, that are applied at a range of orientations to give anisotropic directional derivative (ANDD) filters at each scale [47]. On their own ANDD filters also generate extensions at the end of edge segments, termed edge-stretch, which has the benefit of improving local connectivity by filling in small gaps, particularly at junctions

that occur in the 'Vesselness' filter for example, but with the disadvantage of adding spurious features at the end of edge segments. The latter errors can be minimised by using a fused detector that combines the ANDD filter with a small isotropic Gaussian as a geometric mean [47]. The enhanced edge image is taken as the maximum response at any scale and orientation. These filters give strong responses when aligned to the dominant ridge at each scale, and provide estimates of the ridge intensity and ridge orientation without calculation of the eigenvalues and eigenvectors. In addition, the response at junctions is not attenuated to the same degree as the 'Vesselness' response because of the edge-stretch phenomena. Conversion to a single-pixel wide skeleton then uses local non-maximal suppression to identify key pixels on the ridge centerline, followed by hysteresis thresholding to identify pixels that form the connected skeleton [32, 47].

An alternative strategy was proposed by Steger [49] to identify ridge centre-lines following convolution with first and second order derivatives of (isotropic) Gaussian kernels, to identify the ridge direction and then identifying the position of the centre-line, without segmentation, from the coefficients of a second-order Taylor polynomial fit to the data [49]. Thus, the direction normal to the ridge is determined from the maximum absolute eigenvalue of the Hessian matrix, and the centre-line point determined from the first derivative of a quadratic polynomial along the normal line, with the strength of the ridge given by the second derivative [49]. Using D_a and D_{aa} to represent the first and second partial derivatives along direction a, and (tn_x, tn_y) to represent the normal to the ridge centre-line at distance t, the centre-line point is given by [49]:

$$(p_x, p_y) = (tn_x, tn_y) \qquad (10)$$

where

$$t = -\frac{D_x n_x + D_y n_y}{D_{xx}n_x^2 + 2D_{xy}n_x n_y + D_{yy}n_y^2} \qquad (11)$$

While ridge enhancement can be built on purely intensity-based filters, such as the Hessian or SOAGKs, these have the downside of being sensitive to changes in image contrast, which often leads to loss of a few pixels from the skeleton during the subsequent thresholding step, effectively disconnecting these edges. This can be ameliorated to some extent by inclusion of a local contrast equalisation step prior to enhancement [47], or by the use of adaptive or hysteresis thresholding during segmentation [32], or when linking points in the Steger algorithm [49]. Nevertheless, in these approaches it is critical to establish a reliable, context-dependent threshold selection to achieve segmentation of a fully connected network.

Human observers face a similar challenge when trying to discriminate edges or ridges is a complex visual field.

Morrone and Owens [37] proposed that human edge perception depends on the degree of phase congruency, independent of the brightness. Phase congruency can be estimated from the local energy determined by convolution of the image with Gabor filters at varying scale and orientation [52]. The phase congruency approach has been developed further as a generic means to extract a variety of image features by Kovesi [27, 28]. Kovesi also introduced a range of improvements to the original measure to improve its overall utility, including log Gabor filters to increase the filter bandwidth, procedures for automated noise rejection, weighting to select against phase congruency of only a few frequencies, and improved spatial precision by including both the cosine and sine of the phase in the estimate [27]. These provide good ridge enhancement, irrespective of image intensity, but also increase the number of parameters that can be tuned to achieve the best enhancement in any particular context.

Following Kovesi [27, 28], the local energy for a one-dimensional profile, $I(x)$ is given by:

$$E(x) = \sqrt{F^2(x) + H^2(x)} \qquad (12)$$

where $F(x)$ is the signal with its DC component removed, and $H(x)$ is the Hilbert transform of $F(x)$, obtained by convolving the signal with a quadrature pair of log Gabor filters at scale n, and summing the even filter convolutions ($e_n(x)$) to give $F(x)$, and the odd filter convolutions ($o_n(x)$) to give $H(x)$. The phase congruency $PC(x)$, is normalised by the sum of the Fourier amplitudes $\sum_n A_n(x) \simeq \sum_n \sqrt{e_n(x)^2 + o_n(x)^2}$, with the addition of a small constant ε to improve stability at low Fourier amplitudes:

$$PC(x) = \frac{E(x)}{\sum_n A_n + \varepsilon} \qquad (13)$$

The log Gabor filter bank is controlled by the minimum wavelength scale, the number of scales, the frequency bandwidth, and the number of filter orientations. Each of these requires some optimisation to achieve good enhancement for specific types of biological networks.

The next tuneable parameter controls the amount of noise rejection. To estimate the amount of noise adaptively from the image, Kovesi used a measure of the mean (μ_R) and variance (σ_R^2) of the Rayleigh distribution (R) describing the noise distribution at the smallest scale, with the assumption that ridges are relatively sparsely distributed in the image, so the mean will be dominated by background noise at this scale. Thus the noise threshold (T), is given by the mean noise response plus some number, k, of deviation units:

$$T = \mu_R + k\sigma_R \qquad (14)$$

The local energy term $E(x)$ is therefore modified by subtracting the estimated noise (and setting any values below zero to zero).

The second set of tuneable parameters relate to the minimum spread of frequencies required to constitute a useful estimate of phase congruency. In the case of *Physarum* we are concerned with the detection of ridges, rather than lines or step functions. The expected power spectrum of a ridge falls off at $1/\omega^4$, where ω is the center frequency of the filter, which gives an expected distribution of frequency responses strongly skewed towards low-frequency end. The significance of $PC(x)$ can be down-weighted if the spread of frequencies is too narrow, however, in the case of ridge detection, this criterion should not be too harsh. Kovesi provides an estimate of the frequency spread by considering the normalised ratio of the sum of the Fourier amplitudes divided by the maximum response:

$$s(x) = \frac{1}{N} \left(\frac{\sum_n A_n(x)}{A_{max}(x) + \varepsilon} \right) \qquad (15)$$

Where N is the total number of scales, $A_{max}(x)$ is the maximum filter response at x, and ε prevents division by zero. To penalise regions with few frequency components, the weighting function is constructed as a sigmoidal function:

$$W(x) = \frac{1}{1 + e^{\gamma(c - s(x))}} \qquad (16)$$

where c is the cut-off value below which phase congruency values are penalised, and γ is a gain factor that controls the sharpness of the cutoff.

$$PC(x) = \frac{W(x)\lfloor E(x) - T \rfloor}{\sum_n A_n(x) + \varepsilon} \qquad (17)$$

Where $\lfloor \ \rfloor$ denotes that $E(x) - T$ is equal to itself for positive values and zero otherwise.

The final amendment that Kovesi proposes is to include the information from both the cosine of the phase deviation, which should be large if phase congruency is high, and the absolute value of the sine of the phase deviation, which should be small (18):

$$\Delta\Phi_n(x) = \cos(\phi_n(x) - \bar\phi(x) - |\sin(\phi_n(x) - \bar\phi(x)| \quad (18)$$

This gives the complete estimate of phase congruency as:

$$PC(x) = \frac{\sum_n W(x)\lfloor A_n(x)\Delta\Phi_n(x) - T \rfloor}{\sum_n A_n(x) + \varepsilon} \qquad (19)$$

The two dimensional extension of the phase congruency gives:

$$PC(x) = \frac{\sum_o \sum_n W_o(x)\lfloor A_{no}(x)\Delta\Phi_{no}(x) - T_o \rfloor}{\sum_o \sum_n A_{no}(x) + \varepsilon} \qquad (20)$$

Where o is the index over orientations.

III.   MATERIALS AND METHODS

A.   Establishment of evacuation networks

Plasmodia of *Physarum polycephalum* were grown on a 1% w/v agar (S-7, Ina Food Industry) with oat meal flakes (Quaker) in the dark. Evacuation networks were formed by allowing an excised sheet of protoplasm to exit an enclosed rectangular arena through a single channel in response to addition of a food source according to [1]. Time lapse images were obtained with transmitted light with an (x, y) pixel spacing of $6.2\mu m$, at 1 h intervals and imported into a MATLAB GUI for all subsequent processing steps.

B.   Overview of the network extraction work flow

A flow diagram of the complete network extraction and analysis workflow is given in Fig. 1, and an introduction to the software package is given in the online Supplementary Material. The code available from www.markfricker.org.

In brief, a time-series of images spanning a 4-5h period when the network was forming, typically after 9-10h, were aligned by cross-correlation (Fig. 1A). The minimum vein size was estimated as the full-width half-maximum (FWHM) from a user-defined profile drawn across the image (Fig. 1B), and used to resample the image to ensure that the minimum vein size was consistent (typically 5 pixels wide), and matched to subsequent filtering operation. Images were inverted, background corrected, and smoothed with a guided filter [21], with 5×5 kernel size (Fig. 1C). The median intensity over time was used to construct a single a template image, and veins selectively enhanced using the 'Vesselness' [15], 'Neuriteness' [34], SOAGK [32], Steger curvilinear detector [49], or phase congruency feature type [27, 28, 39]. The Steger algorithm automatically yields a single-pixel wide skeleton. For the other methods, an h-minimum transform [48] was used to suppress background regions containing noise. A single-pixel wide skeleton was extracted using a watershed algorithm [35], to ensure full connectivity, or using hysteresis thresholding with manually adjusted thresholds. Hysteresis thresholding is required if there are free ends present, but also risks disconnecting edges that fall below the minimum threshold. The boundary of the arena was used to define a binary mask that was imposed on the template (Fig. 1D), whilst the exit region and food source were defined as a 'feature' used to set the identity of the node in the graph representing the exit point (node 0) (Fig. 1E). The polygonal regions between the veins were segmented from the complement of the pixel skeleton (Fig. 1F), which allowed various morphological metrics to be calculated for each inter-vein region.

C.   Comparison with ground-truth

Pixel skeletons for each ridge enhancement-skeletonisation combination were scored against a manually digitised ground-truth (Fig. 1G), with a tolerance of half the minimum vein width for true positives (TPs), true negatives (TNs), false positive (FPs), and false negatives (FNs) [31]. Results were combined using Precision-Recall (PRC) analysis, where Precision was calculated as TP/(TP+FP), and Recall as TP/(TP+FN). PRC was used in preference to Receiver Operating Characteristic (ROC) plots, as the former are better suited to imbalanced datasets [45], such as *Physarum* networks, when the number of true negatives (TNs) from the background is expected to be much greater than the true positives (TPs) from the skeleton. As all the algorithms have several tuneable parameters, including intensity thresholds or the h-minimum threshold, PRC analysis was used as a guide to parameter optimisation by combinatorial evaluation of parameter settings, with the PRC curve constructed by tuning the segmentation threshold parameter. The best performance was assessed from the highest F_β score representing a harmonic mean of recall and precision. F_β, can also be tuned to weight recall ($\beta = 2$) or precision ($\beta = 0.5$) more:

$$F_\beta = (1 + \beta^2) \frac{\text{Precision} \times \text{Recall}}{(\beta^2 \times \text{Precision}) + \text{Recall}} \quad (21)$$

D.   Conversion to a weighted graph

The width of the veins and intervening plasmodial sheet at each pixel was estimated using the Lambert-Beer law (Fig. 1H) as $k \log_{10}(I_0/I)$, where I_0 was the incident light intensity, I the transmitted light intensity, and k a calibration coefficient based on the absorbance of the filled arena at the start where the path length was fixed at $170\mu m$. The pixel skeleton was then converted to a graph G, (Fig. 1J) with N nodes and M edges, where edge ij represents a vein segment between two junctions or a junction and free end, denoted as node i and node j. The graph was adjusted to accommodate any features, by placing a new node at the centroid of the feature, connected to each edge incident on the boundary (Fig. 1K). A dual-graph for the inter-vein regions was constructed that linked each polygonal region to its neighbours, with the strength of the edge determined by the width of the intervening vein (Fig. 1L).

E.   Measurement of graph metrics

Each edge was associated with a vector of features including the average intensity ($\bar{I}_{ij}$), length (l_{ij}), and average width (w_{ij}), determined by excluding pixels that
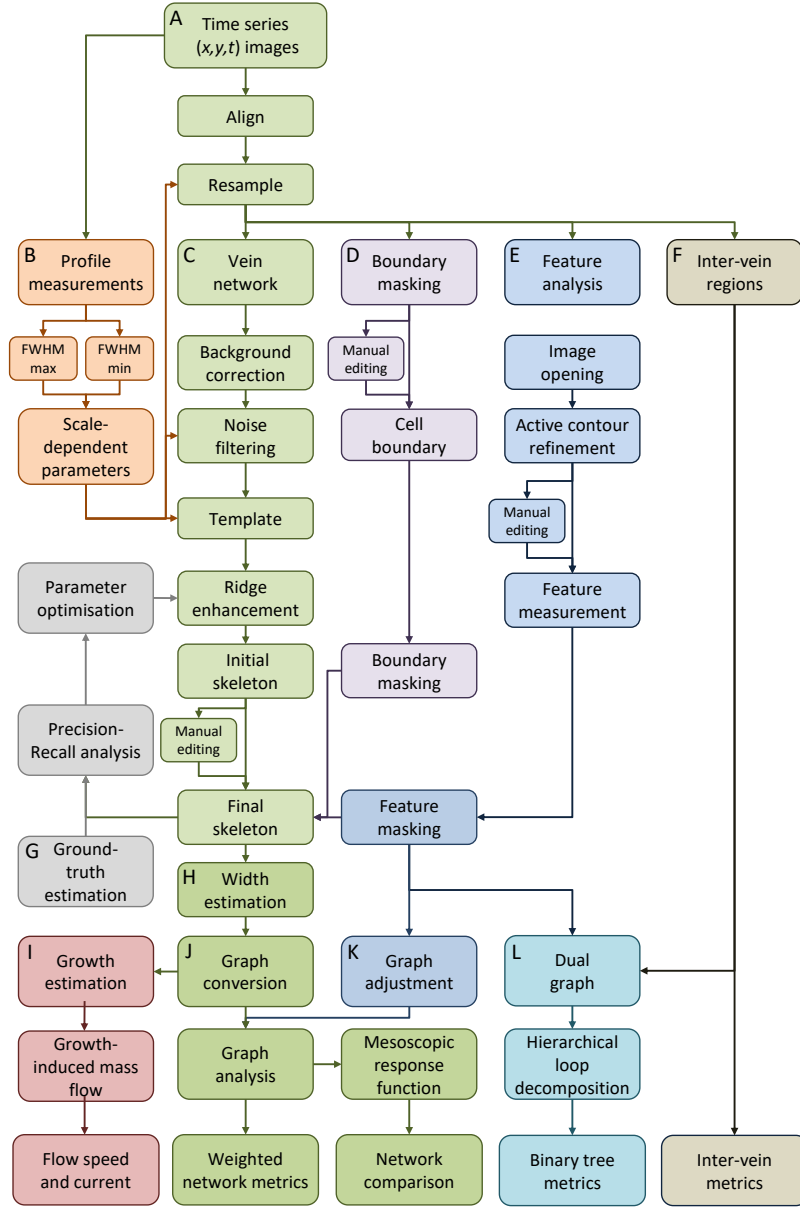
FIG. 1: (Colour on-line) Flow diagram of the main steps in automated extraction and analysis of *Physarum* networks

overlapped with any larger veins at the end of the edge, to give a centre-weighted estimate, more representative of the vein itself. The centre-weighted width was used to calculate the radius (r_{ij}), area ($a_{ij} = \pi r_{ij}^2$), volume ($v_{ij} = a_{ij}l_{ij}$), predicted resistance to flow or drag [2] ($\theta_{ij} = l_{ij}/r_{ij}^4$). The position of each node in the arena was used to calculate the Euclidean distance from the exit point, denoted as node_0, (d_{i0}), and the hydraulic accessibility to the exit point [1, 2], measured as the path of minimum resistance, calculated using Dijkstra's algorithm. The edge betweenness centrality β_u for edge u was calculated as the proportion of all shortest paths (σ_{iuj}) between pairs of nodes i and j, that pass through

u (Equation 22), to give a measure of the importance of a node or link to transport. Loss of the node or link with the highest betweenness centrality leads to the greatest increase in shortest path lengths.

$$\beta_u = \sum_{ij} \frac{\sigma_{iuj}}{\sigma_{ij}} \tag{22}$$

These measures were used to calculate summary statistics for the network, including the route factor [19], defined as the average path length to the exit point divided by the Euclidean distance:

$$q = \frac{1}{N-1} \sum_{i=1}^{N-1} \frac{l_{i0}}{d_{i0}} \qquad (23)$$

The global efficiency [29], defined as the mean reciprocal of the shortest paths, weighted by resistance, with the reciprocal for disconnected nodes defined as zero (Equation 24), and the root efficiency (E_{root}) was calculated in a similar manner from the exit point to all other nodes.

$$E_{global} = \frac{1}{N(N-1)} \sum_{i \neq j \in G} \frac{1}{d_{ij}} \qquad (24)$$

The α-coefficient [20] or meshedness [9] was used to measure the fraction of links present compared to a fully connected planar network, taking values from 0 to 1 to allow comparison of networks of different sizes:

$$\alpha = \frac{M - N + G}{2N - 5} \qquad (25)$$

Graphs were also output for investigation using community detection algorithms and mesoscopic response functions for comparison with networks in other domains [30, 40], but are not described further here.

F. Hierarchical network decomposition

The overall structure of the *Physarum* network was investigated using hierarchical loop decomposition [26, 36] of the dual-graph (Fig. 1L). In this implementation, the areas that were separated by the thinnest edge were fused first, then the areas separated by the second thinnest edge, and so on. Both the initial areas and the areas formed by fusions were represented as nodes in the dual-graph of the vein network, and these nodes were connected if the areas in question were formed by this hierarchical, fusion process. Note that by construction, the dual graph of the vein network is a binary tree.

G. Analysis of predicted flows

The difference in vein volume between two time points was used to estimate the volumetric current flow through the network exiting the arena [23, 24] (Fig. 1I). Veins that thin over time are the source of protoplasmic volume, while thickening veins are sinks. To accommodate flows of material from any plasmodial sheet remaining in the inter-vein regions, the volume change for each pixel in the inter-vein region was also allocated to the nearest edge in the network, based on the Euclidean distance map (EDM) from the pixel skeleton. The net difference in volume for all veins and inter-vein regions was assumed to exit the arena to conserve mass. Assuming the volume

of vein ij decreases from u_{ij} to v_{ij} over time t, the current flowing out of vein ij must be $(v_{ij} - u_{ij})/t$ greater than the current flowing into vein ij. As a simplifying assumption, half the net current was allocated to node i, and half to node j. To make an unbiased analysis of the relationship between current and changes in cross-sectional area, the current induced in vein ab by the changes in volume of the all the veins was calculated excluding vein ab itself. Thus, the net current flowing out of node i was defined as:

$$q_i = \begin{cases} -\sum_{j \neq i} q_j & \text{if node } j \text{ is the exit,} \\ \sum_{ij \neq ab} \frac{u_{ij} - v_{ij}}{2t} & \text{otherwise.} \end{cases} \qquad (26)$$

Note that the first sum is over the set of all nodes, while the second sum is over the set of all the veins ij directly connected to node i. The net current flowing out of each node and the conductance of each vein uniquely determine the pressure difference between any pair of nodes [24]. Given a pressure drop ΔP between the end points of a vein of length l and radius r, the current Q through the vein follows equation (27), where ν is the dynamic viscosity of the cytoplasm:

$$Q = \frac{\pi r^4}{8 \nu l} \Delta P \qquad (27)$$

Given the net current at each node and the hydraulic conductance of each vein, we calculated the unique current [24] in each vein that was consistent with equations (26) and (27). We have previously examined the scaling relationship between parent and daughter vessel radii at three-way junctions [1] to test whether *Physarum* networks obey Murray's law [38]. This predicts that the radius r_0 of a parent vessel is related to the radii of the daughter vessels r_1 and r_2 by the relationship:

$$r_0^3 = r_1^3 + r_2^3 \qquad (28)$$

Here we extend this analysis to test the predicted scaling relationships with vein radius based on flow through the entire network, specifically volumetric flow ($\propto r^3$), speed ($\propto r^1$), and shear force ($\propto r^0$) [46].

IV. RESULTS

A. Evaluation of different ridge enhancement methods in *Physarum*

A typical vein network for *Physarum* exiting a square arena is shown in Fig. 2A, where a branching tree with many loops has formed as the plasmodium re-deploys biomass from the arena via a single exit channel located at the bottom of the image in Fig. 2A.
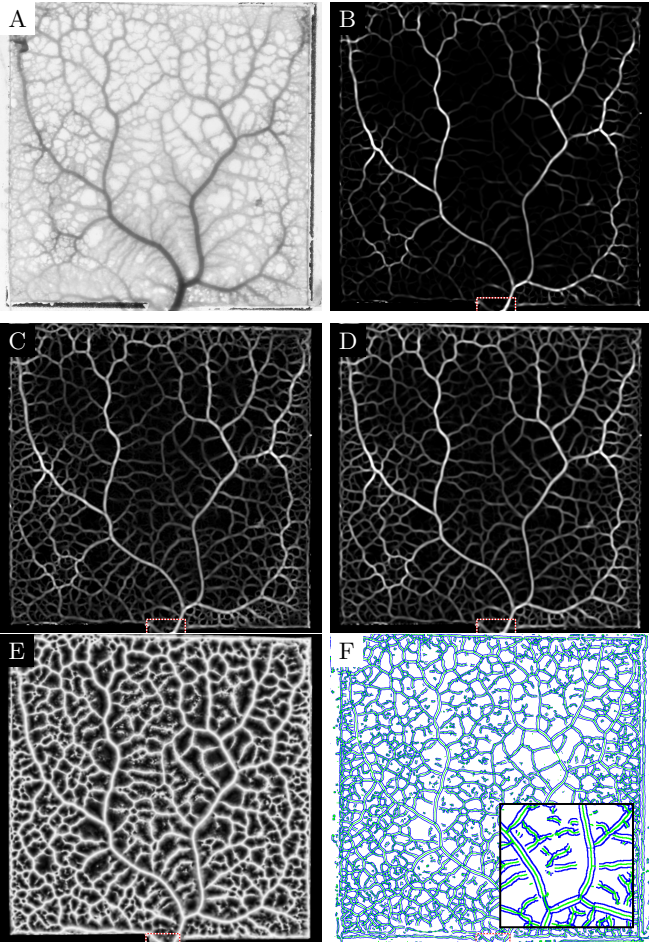
FIG. 2: (Colour on-line) Automated analysis of a *Physarum* network evacuating from a 10×10 mm square arena through a single exit point. (A) Original image; (B) ridge enhancement using the 'Vesselness' algorithm [15]; (C) 'Neuriteness' algorithm [15];(D) second-order anisotropic Gaussian kernel (SOAGK) [32, 47]; (E) local weighted mean phase angle ('Feature Type', FT) from phase congruency [27, 28, 39]; and (F) Steger algorithm [49], where the center-line is marked in green and the width in blue. the inset shows an enlarged region, where edges fail to connect to the main vein where the plasmodial sheet is not yet well resolved into separate veins

The results of ridge enhancement are shown for the 'Vesselness' filter (Fig. 2B), 'Neuriteness' filter (Fig. 2C), second-order anisotropic Gaussian filter (SOAGK, Fig. 2D), local weighted mean phase angle (termed the 'Feature Type') calculated from the phase congruency (Fig. 2E), and the Steger algorithm (Fig. 2F). The 'Vesselness' filter provided good smoothing and enhancement of the major veins, but gave low contrast for the minor veins. In addition, information was lost at the junctions and branch points, that led to disconnection of elements in the skeleton unless a very low threshold was chosen. The 'Neuriteness' (Fig. 2C) and SOAGK filters (Fig. 2D) also gave good smoothing, improved con-

trast of minor veins, and were less susceptible to errors at junctions. However, all three methods retained much of the original intensity information in the strength of the ridges, making subsequent intensity-based segmentation steps sensitive to the absolute threshold values used. The phase congruency 'Feature Type' image gave a strong response for all sizes of veins, independent of their original intensity, but also gave spurious responses to noise in the background (Fig. 2E). The Steger algorithm calculated the position of ridge centre-line directly from the minimum ratio of the first and second derivatives drawn normal to the ridge centreline (Fig. 2F, green), and also estimated the width (Fig. 2F, blue). However, veins were often disconnected in regions where the plasmodial sheet was not yet well resolved into separate venules (Fig. 2F, inset).
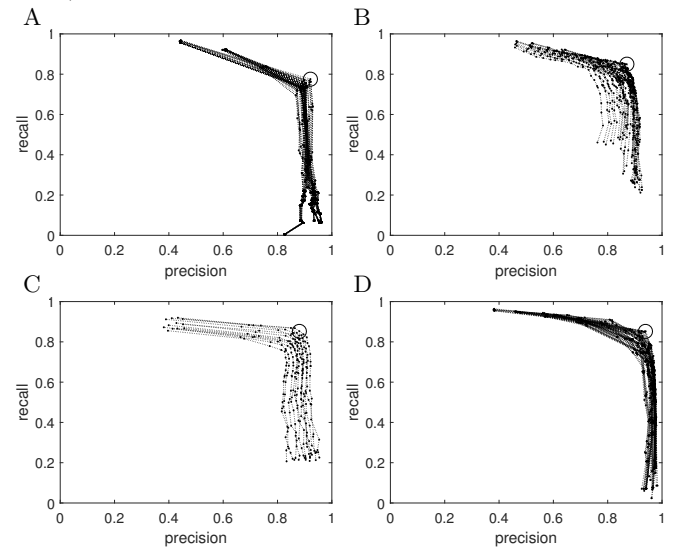

FIG. 3: Precision-Recall plots for factorial parameter combinations using (A) the 'Vesselness' algorithm; (B) 'Neuriteness' algorithm; (C) SOAGK; or (D) phase congruency 'Feature Type'. The circled point represents the combination that gives the highest overall F_1 value.

In each case, parameter values were optimised by systematically testing factorial combinations of parameter values, and comparing the resultant pixel skeleton to a manually-determined ground truth using Precision-Recall (P-R) plots (see Fig. 3 and Fig. 4). In all cases, parameter combinations could be found that yielded comparable overall performance (Table I), although the sensitivity of the final result to perturbation of each parameter differed between the methods (Fig. 3), indicated to some extent by the spread between successive P-R plots.

Comparison with the ground-truth aided parameter selection. furthermore, the F_β criteria used to evaluate PRC performance can itself be further weighted in favour of avoiding false negatives (FN), to offset the consequences of losing a pixel that should be part of the skeleton. FNs have a much greater impact on connectivity than the risk of including some background pixels in
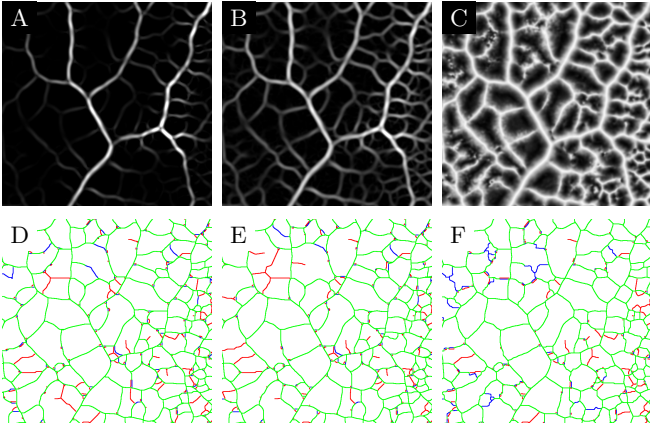
FIG. 4: (Colour on-line) Spatial mapping of Precision-Recall analysis following parameter optimisation and watershed segmentation for a small region-of-interest using the 'Vesselness' algorithm (A,D); SOAGK (B,E); and Feature Type (C,F). In the pixel skeletons (D-F), green represents pixels that match the ground-truth (GT) within a 3 pixel tolerance ($\sim 19\mu m$), red pixels are false negatives (FNs) that are present in the GT, but not the segmented skeleton, whilst blue pixels are false positive (FPs), present in the skeleton, but not in the GT.

a false edge (compare, for example FT (F_1) and FT (F_2) in Table I).

TABLE I: Typical Precision-Recall analysis of different ridge enhancement and segmentation algorithms. Each algorithm was run with a factorial set of different parameter combinations (comb.). Results are shown for the highest F_1 score for all algorithms, and for the highest F_2 score, which weights Recall higher than Precision, for the Feature Type.

	Vesselness	Neuriteness	SOAGK	Feature Type (F_1)	Feature Type (F_2)
comb.	180	35	45	324	324
TP	6,545	7,466	8,072	7,229	7,937
FP	796	1,116	985	464	1,642
FN	2,030	1,322	695	1,250	740
TN	278,980	278,450	278,600	279,910	278,040
Prec.	0.89	0.87	0.89	0.94	0.83
Recall	0.76	0.85	0.92	0.85	0.91
F1	0.82	0.86	0.91	0.89	0.9

B. Analysis of the tubule network

The evacuation networks examined here progress from a fully-connected network to a branching system, eventually leaving some free ends as they regress completely from the arena. As the veins do not shift their position laterally, a single fully-connected skeleton was determined from the median projection of the time series, following 'Feature Type' enhancement and watershed segmentation. The skeleton was then used to interrogate the intensity image at each time point. This ensures that each node and edge in the graph retained its unique identity throughout the time series, even if the width tended to zero as the edge was removed. In other situations, hysteresis thresholding and thinning of the resultant binary image can be used to give a pixel-based skeleton that includes free ends, but this method of segmentation is much more sensitive to the hysteresis thresholds used.
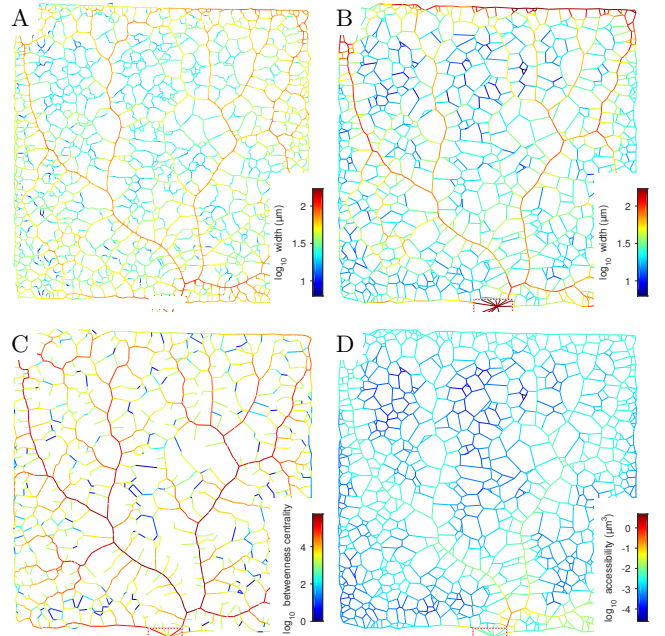

FIG. 5: (Colour on-line) Conversion from a pixel skeleton to a weighted graph. (A) single pixel-wide pixel skeleton, colour coded by local vein thickness; (B) graph representation with nodes at junctions and edges colour-coded by average vein thickness; (C) network graph colour-coded by betweenness centrality; (D) network graph colour-coded by hydraulic accessibility.

The width (w) at each pixel was estimated following calibration of the each intensity image using the Lambert-Beer law (Fig. 5A). The pixel-skeleton was then converted to a graph representation with nodes at the junctions and free ends (if present), connected by edges that were weighted by length (l) and width (w) (Fig. 5B). The volume of plasmodial sheet in the region adjacent to each vein was also calculated from the Lambert-Beer law and any change in volume was allocated to the nearest edge. The graph was further modified to accommodate additional features, such as the location of resources. Standard graph-theoretic metrics were then calculated, including the node or edge betweenness centrality (Fig. 5C). In addition, spatially relevant network measures were determined, such as the euclidean distance from exit point in the boundary of the experimental arena, or the hydraulic accessibility (Fig. 5D), defined as the average shortest path weighted by resistance from the exit to the end nodes of each edge. Typically the

architecture of the network conferred a similar predicted evacuation time irrespective of Euclidean distance from the exit point (Fig. 5D), confirming previous results for manually delineated networks [1].

C.   Network metrics

Plasmodia evacuating the different arena shapes typically formed networks with 2200-2500 edges connecting 1400-1800 nodes (Table II), giving an edge:node ratio of 1.497±0.006, with an overall length of 500-600 mm, giving a vein density of 5-6 mm mm^{-2}, a node density of 15-17 nodes mm^{-2}, and a polygon density of ∼8 polygons mm^{-2}, with polygons showing consistently high circularity (Table II). The node degree (k=3) was un-informative in these networks, as the watershed segmentation ensures that there are no k=1 nodes, except for the edges incident on the feature, and k>3 nodes are extremely rare. Vein length followed an approximate log-normal distribution, with a slight skew towards shorter values (Fig. 6A). Note vein length does not change in these experiments, as the network structure was constrained to the same skeleton at each time point (see Materials and Methods). The average and median vein lengths were around 200-250 μm for all the different arena sizes, and were fairly straight, with a low tortuosity (Table II). Vein widths and vein volumes followed a log-normal distribution (Fig. 6B and C, respectively), that decreased from 10h (black bars) to 13h (white bars), as the network evacuated the arena. The average width at 10h ranged from 46-64 μm, with larger values associated with an increasing width-to-height aspect ratio in the arena (Table II). As the total vein length was similar between arenas, this also resulted in different network volumes at the 10h time point (Fig. 6C). Vein resistance or drag increased as the networks evacuated (Fig. 6D). One factor that impacts on the performance of the network is the number of cross-links present. In all arenas, the α-coefficient or 'meshedness' was around 0.25, meaning around 1 in 4 of the maximum number of cross-links expected for a planar network were present. Another way to express the impact of additional edges is to compare the total length of network with the minimum spanning tree (MST), which was remarkably consistent at just under 0.5 for all arena shapes (Table II).

Neither meshedness nor MST-ratio consider the widths of the edges, which may give a misleading view of the importance of different paths through the network. By contrast, the global transport efficiency (E_{global}) between all nodes, calculated as the sum of the inverse of all shortest paths normalised to the number of nodes, showed that the network architecture in the different systems had an impact on the predicted overall transport efficiency (Table II). This difference was less pronounced when only transport efficiency to the exit node (root efficiency, E_{root}) was considered (Table II), which is perhaps more representative of the biological situation in these arenas.

The edge betweenness centrality (B_u), calculated on the basis of vein length alone followed a log-normal distribution (Fig. 6E, open bars). However, B_u calculated for vein resistance, showed a more complex distribution (Fig. 6E, closed bars). Thus, a few edges had a very low β_u, and were likely to disappear, whilst the remainder followed a high-power exponential distribution. The hydraulic accessibility (Fig. 5F), measured as the path of least resistance from the exit point to every node, fell away from the exit point, but then showed a relatively similar behaviour across the entire network irrespective of the distance from the exit point (Fig. 6F).
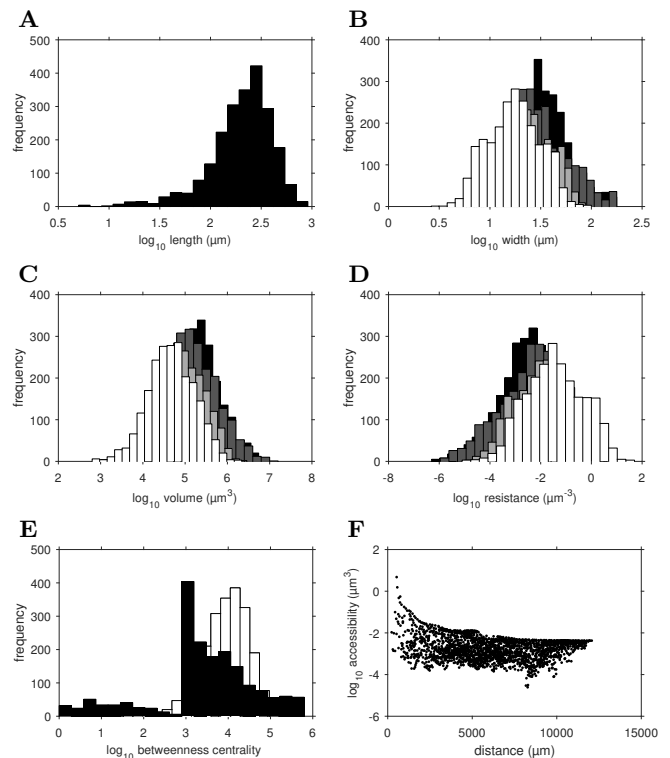

FIG. 6: Distributions of key network measurements. (A) vein length; (B) vein width; (C) vein volume; (D) vein resistance; (E) vein betweenness centrality based on length (open bars) or resistance (closed bars); and (F) Hydraulic accessibility, measured as the inverse of the path of least resistance to the exit.

D.   Dual-graph of the intervening polygonal areas

The area of the polygonal regions between the veins (Fig. 7A), followed a right skewed log-normal distribution (Fig. 7C), although the lower end of the distribution was critically dependent on how well the initial pixel skeleton subdivided the plasmodial sheet at the finest scale. The maximum distance within any region to the skeleton was normally distributed, with a mean around 110μm. A more powerful hierarchical decompo-

TABLE II: Network metrics for five different rectangular arenas

	Rectangle 1	Rectangle 2	Rectangle 3	Rectangle 4	Rectangle 5
size (mm)	6×17.5	7.5×14.5	10×10	14×7.3	20×5
replicates	5	4	5	5	4
number of veins	2243 ± 262	2712 ± 454	2205 ± 211	2515 ± 128	2304 ± 353
number of nodes	1498 ± 175	1811 ± 302	1475 ± 141	1681 ± 86	1538 ± 235
number of polygons	744 ± 87	902 ± 152	730 ± 70	833 ± 43	766 ± 117
node degree	2.99 ± 0.002	2.99 ± 0.005	2.98 ± 0.005	2.99 ± 0.003	2.99 ± 0.00
total length (mm)	531 ± 33	599 ± 58	551 ± 24	598 ± 17	578 ± 43
vein density (mm mm^{-2})	5.84 ± 0.28	5.67 ± 0.57	5.56 ± 0.29	5.96 ± 0.15	5.76 ± 0.41
node density (mm^{-2})	16.4 ± 1.7	16.3 ± 3.2	14.9 ± 1.5	16.7 ± 0.8	15.7 ± 2.2
polygon density (mm^{-2})	8.16 ± 0.85	8.13 ± 1.62	7.38 ± 0.76	8.30 ± 0.40	7.81 ± 1.10
area circularity	0.78 ± 0.01	0.79 ± 0.01	0.78 ± 0.01	0.78 ± 0.01	0.79 ± 0.01
mean vein length (μm)	242 ± 12	246 ± 25	255 ± 14	239 ± 6	253 ± 18
median vein length (μm)	211 ± 11	213 ± 23	224 ± 13	214 ± 6	227 ± 19
tortuosity	1.10 ± 0.01	1.09 ± 0.004	1.09 ± 0.002	1.09 ± 0.01	1.09 ± 0.003
mean vein width (μm)	46.4 ± 3.4	48.8 ± 5.2	47.2 ± 3.9	63.9 ± 5.7	57.7 ± 8.8
median vein width (μm)	36.2 ± 3.7	36.9 ± 3.9	35.9 ± 2.7	54.6 ± 6.0	48.2 ± 8.7
total volume (mm^3)	0.72 ± 0.10	0.64 ± 0.11	0.74 ± 0.09	1.10 ± 0.19	1.05 ± 0.19
meshedness	0.25 ± 0.0002	0.25 ± 0.001	0.25 ± 0.001	0.25 ± 0.001	0.25 ± 0.0001
MST ratio	0.47 ± 0.01	0.47 ± 0.003	0.48 ± 0.003	0.47 ± 0.002	0.48 ± 0.01
global efficiency (mm^3)	137 ± 25	104 ± 29	141 ± 33	327 ± 74	267 ± 97
root efficiency (mm^3)	1278 ± 67	1016 ± 308	1048 ± 140	1707 ± 597	1486 ± 708

sition analysis [26, 36] was based on the dual-graph of the vein network with the edge weights between adjacent regions determined by the width of the common vein (Fig. 7B). A binary tree was constructed by successively fusing polygonal regions in sequence depending on the thickness of the intervening edge. The terminal nodes in the tree represent each original inter-vein region, and the pattern of fusions led to aggregation into larger regions in a characteristic hierarchical manner (Fig. 7E).

E. Prediction of long-term flow dynamics

Over short time intervals (hours), the spatial position of the tubes did not vary significantly, but their diameter changed in response to both short-term shuttle-streaming, and longer-term re-modelling of the network architecture as it exited the arena. It was therefore possible to track changes in each part of the network by re-applying the same network extraction routine to successive images using a skeleton based on the median network present in the time window considered. Such time-dependent changes in tube volume were used to predict the net mass flow through the tubular network. Material flowing to or from the sheet-like regions between the veins or at the growing margin of the plasmodium were included in the flow models by allocating their change in volume to the nearest tube.

The predicted current was determined from the volume flow in each edge, and the resultant speed and shear forces calculated from the cross-sectional area. Colour-coded maps of the $\log_{10}$ absolute values are shown for volume change between 10h and 11h (Fig. 8A), the predicted current (Fig. 8B), speed (Fig. 8C), and shear force (Fig. 8D), with the corresponding regression of each parameter against $\log_{10}$ tube radius in (Fig. 9A-C). If the

entire system follows expectations from Murray's law, the slope of the regression lines would be expected to be 3, 1 and 0, respectively. Results for all the networks, grouped by the arena size, are shown in (Fig. 9D), and follow expectations well.

V. DISCUSSION

A number of scale-space ridge enhancement techniques were examined to improved network extraction from an initially homogeneous plasmodial sheet of *Physarum* as it evacuated a rectangluar arena with different aspect ratios. By comparison with a ground-truth skeleton using precision-recall analysis, it was possible to optimise the enhancement and segmentation parameters for each method to give a reasonable pixel skeleton, particularly when combined with watershed segmentation that ensures edges remain connected. The disadvantage of the watershed approach was it excludes veins with free ends. These could be extracted using hysteresis thresholding, however, all the intensity-based methods ('Vesselness' [15], 'Neuriteness' [34], SOAGK [32, 47]) were very sensitive to the precise threshold used. By contrast, the 'Feature Type' output from the phase congruency method [27, 28, 39] delivered a high-contrast enhanced ridge image, that was insensitive to the initial intensity variation from the different size veins or sheet regions. This made segmentation by either watershed or hysteresis thresholding tolerant of the threshold value, and added robustness to the overall processing pipeline. The alternative Steger algorithm [49] that finds the center-line and vein width without explicit segmentation, performed well over large regions of the network, by failed at critical junctions where the veins were still emerging from the intervening plasmodial sheet. Nevertheless, there may be merit in
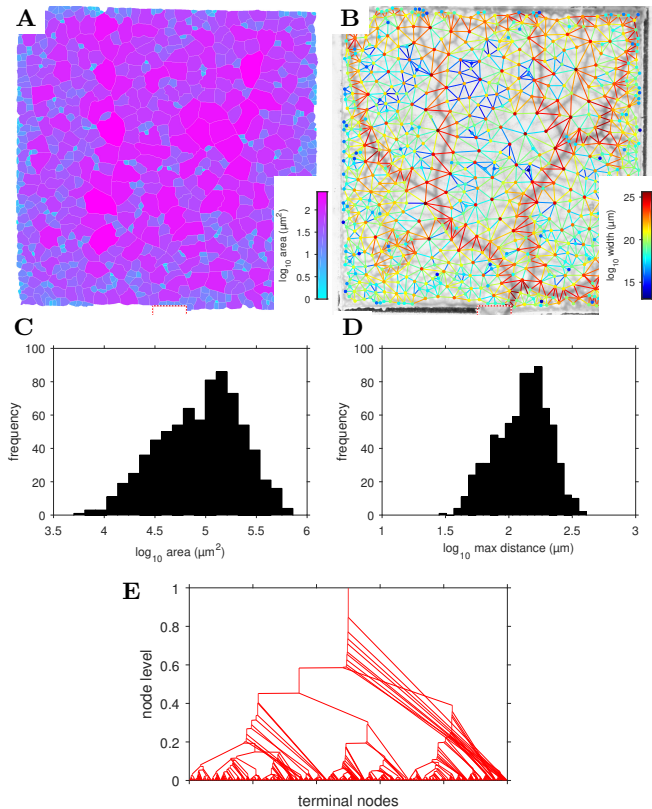
FIG. 7: (Colour on-line) (A) Measurement of the inter-vein areas; (B) Dual graph connecting areas via adjacent edges, colour coded by the edge width; (C) Distribution of inter-vein areas; (D) Distribution of the maximum distance to the skeleton from within each region; (E) Conversion of the dual graph to a branching tree by fusing areas following removal of edges in inverse order of their width.
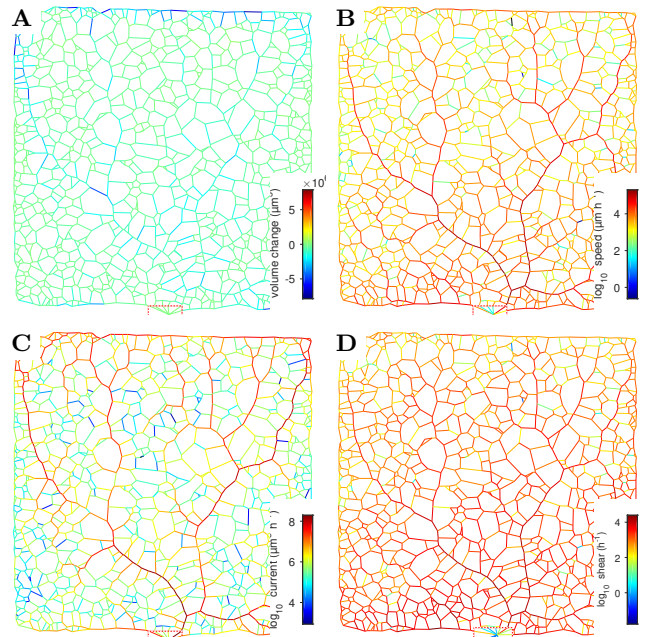

FIG. 8: (Color on-line) Predicted volumetric flows of protoplasmic material over a 1h time interval. (A) Change in volume; (B) Predicted speed; (C) Predicted current; (D) Predicted shear force

combining the ridge-finding and contour linking elements of the Steger algorithm with the intensity-independence of the phase-congruency algorithm.

The initial images used here were collected from smaller arena sizes (100 mm^2), but at 7-15$\times$ the spatial resolution (6.2 μm pixel^{-1}) of previous studies on network formation in *Physarum* [2–5, 25], or 2$\times$ that of Fessel *et al.* [13, 14]. This enabled segmentation and analysis of much smaller veins and a more complete distribution of veins widths (6). Equally, the spatial scale, image resolution, network volume, and distribution of vein widths were comparable to the excised networks used by Marbach *et al.* [33], although as the latter networks were already well established, they could be segmented by simple intensity-based thresholding.

As a result of the increased resolution, other network parameters, such as the meshedness (0.25), were higher than previous estimates (0.1-0.15, [25]) for *Physarum*, more closely resembling a hexagonal lattice. The meshedness is somewhat lower in other biological systems, typi-

cally in the range 0.04-0.29 for ant galleries [9] or 0.11-0.2 for fungal networks [6], but closer to that observed for road networks in cities [10, 11].

Estimates of the resistance to flow or drag extended over a greater range than previous reports [2], particularly for low resistance vein segments, probably because in these early developing networks the individual vein lengths were shorter. The converse was true for the hydraulic accessibility, which is the reciprocal of the sum of resistances to the exit from each node, and therefore includes the total length of all the vein segments on the shortest path, including very fine veins. Thus average values to the exit were typically in the $10^{-2} - 10^{-4} \mu$m^{-3} range here, compared to $10^0 - 10^{-2}$ for coarsening networks [2]. The global and root efficiency measures summarise the predicted transport behaviour of the network. The root efficiency to the exit is probably the most useful measure for evacuation networks, and showed a slight increase as the aspect ratio of the arena decreased. We note that E_{global} and E_{root} used here are for shortest paths weighted by resistance [6, 17, 18], rather than on length alone [14], with units of μm^3. However, whilst this may be a more appropriate indicator for the predicted transport behaviour of the network, it cannot then be normalised by the geodesic distance to obtain a dimensionless ratio [14], which may be a more useful comparative indicator between systems.

The average predicted speed for the exit of protoplasm, averaged over 1h intervals, was a few mm h^{-1}, which was at least an order of magnitude slower than for peri-
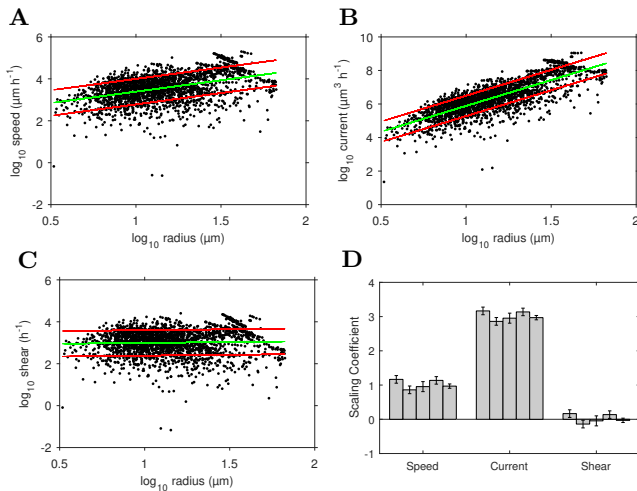
FIG. 9: (Colour on-line) Scaling relationship between radius and (A) Predicted speed with the green lines represent the best-fit linear regression and the red lines ±50% prediction confidence limits; (B) Predicted current; (C) Shear force; (D) Summary of the slopes of the regression for each of the five experimental arenas (mean± s.e.m.). The coefficients are close to predictions from Murray's law, although the spread in each is significant for each parameter at any given radius.

staltic flows responsible for rapid shuttle streaming that operate on a minutes time scale [33]. Indeed, it is likely that changes in vessel diameter due to shuttle streaming are one of the major sources of error in the estimate of vein thickness that lead to the wide variation in predicted speed for any given vein radius. Nevertheless, the trend across all veins matched the scaling exponents predicted from Murray's law, and provide further support that temporal evolution of vein radii may be responding to a internal shear threshold [1].

Acknowledgments

[1] D. Akita, I. Kunita, M. D. Fricker, S. Kuroda, K. Sato, and T. Nakagaki. Experimental models for murray's law. *Journal of Physics D*, 50, 2017.

[2] W. Baumgarten and M. J. B. Hauser. Functional organization of the vascular network of physarum polycephalum. *Physical Biology*, 10, 2013.

[3] W. Baumgarten and MJ Hauser. Detection, extraction, and analysis of the vein network. *J. Comput. Interdiscip. Sci*, 1:241–249, 2010.

[4] W. Baumgarten and M.J.B. Hauser. Computational algorithms for extraction and analysis of two-dimensional transportation networks. *J. Comput. Interdiscip. Sci*, 3: 107–16, 2012.

[5] W. Baumgarten, T. Ueda, and M. J. B. Hauser. Plasmodial vein networks of the slime mold physarum polycephalum form regular graphs. *Phys. Rev. E*, 82, 2010.

[6] Daniel P Bebber, Juliet Hynes, Peter R Darrah, Lynne Boddy, and Mark D Fricker. Biological solutions to transport network design. *Proc. Roy. Soc. B*, 274:2307–2315, 2007.

[7] M. Beekman and T. Latty. Brainless but multi-headed: Decision making by the acellular slime mould physarum polycephalum. *J. Mol. Biol.*, 427:3734–3743, 2015.

[8] L. Boddy, J. Wood, E. Redman, J. Hynes, and M. D. Fricker. Fungal network responses to grazing. *Fungal Genetics and Biology*, 47:522–30, 2010.

[9] J. Buhl, J. Gautrais, R.V Solé, P. Kuntz, J.-L. Valverde, S.and Deneubourg, and G. Theraulaz. Efficiency and robustness in ant networks of galleries. *Eu. Phys. J. B*, 42:123–129, 2004.

[10] J. Buhl, J. Gautrais, N. Reeves, R. V. Solé, S. Valverde, P. Kuntz, and G. Theraulaz. Topological patterns in

street networks ofself-organized urban settlements. *Eu. Phys. J. B*, 49:513–522, 2006.

[11] A. Cardillo, S. Scellato, V. Latora, and S. Porta. Structural properties of planar graphs of urban street patterns. *Phys. Rev. E*, 73:066107, 2006.

[12] M. Dirnberger, T. Kehl, and A. Neumann. Nefi: Network extraction from images. *Scientific Reports*, 5:15669, August 2015.

[13] A. Fessel, C. Oettmeier, E. Bernitt, N. C. Gauthier, and H. G. Dobereiner. Physarum polycephalum percolation as a paradigm for topological phase transitions in transportation networks. *Physical Review Letters*, 109, 2012.

[14] A. Fessel, C. Oettmeier, and H. G. Dobereiner. Structuring precedes extension in percolating physarum polycephalum networks. *Nano Communication Networks*, 6: 87–95, 2015.

[15] A. F. Frangi, W. J. Niessen, K.L. Vincken, and M.A. Viergever. *Multiscale vessel enhancement filtering*, pages 130–137. Springer Berlin Heidelberg, Berlin, Heidelberg, 1998.

[16] W.T. Freeman and E.H. Adelson. The design and use of steerable filters. *IEEE Trans. Pattern Analysis and Machine Intelligence*, 9:891–906, 1991.

[17] M. D. Fricker, J. A. Lee, D. P. Bebber, M. Tlalka, J. Hynes, P. R. Darrah, S. C. Watkinson, and L. Boddy. Imaging complex nutrient dynamics in mycelial networks. *Journal of Microscopy*, 231:317–331, 2008.

[18] M. D. Fricker, L. Boddy, T. Nakagaki, and D. P. Bebber. Adaptive biological networks. *Adaptive Networks: Theory, Models and Applications*, pages 51–70, 2009.

[19] M.T Gastner and MEJ Newman. Shape and efficiency in spatial distribution networks. *J. Stat. Mech.*, 2006:

P01015, 2006.

[20] P Haggett and RJ Chorley. *Network Analysis in Geography (pp 74-76) Edward Arnold Publishers Ltd.* London, 1969.

[21] K. He, J. Sun, and X. Tang. Guided image filtering. *IEEE Transactions on Pattern Analysis and Machine Intelligence*, 35:1397–1409, 2013.

[22] L. Heaton, B. Obara, V. Grau, N. Jones, T. Nakagaki, L. Boddy, and M.D. Fricker. Analysis of fungal networks. *Fungal Biology Reviews*, 26:12–29, 2012.

[23] L. L. Heaton, E. Lopez, P. K. Maini, M. D. Fricker, and N. S. Jones. Advection, diffusion, and delivery over a network. *Phys Rev E*, 86:021905, 2012.

[24] L. L. M Heaton, E Lpez, P. K Maini, M. D Fricker, and N. S Jones. Growth-induced mass flows in fungal networks. *Proc. R. Soc. B*, 277:3265–3274, 2010.

[25] M. Ito, R. Okamoto, and A. Takamatsu. Characterization of adaptation by morphology in a planar biological network of plasmodial slime mold. *Journal of the Physical Society of Japan*, 80, 2011.

[26] E. Katifori and M.O. Magnasco. Quantifying loopy network architectures. *PLoS One*, 7:e37994, 2012.

[27] P. Kovesi. Image features from phase congruency. *Videre: Journal of Computer Vision Research*, 1:1–26, 1999.

[28] P. Kovesi. Phase congruency: A low-level image invariant. *Psychological Research*, 64:136–148., 2000.

[29] V. Latora and M. Marchiori. Efficient behavior of small-world networks. *Phys. Rev. Lett.*, 87:198701, 2001.

[30] S.-H. Lee, M.D. Fricker, and M.A. Porter. Mesoscale analyses of fungal networks as an approach for quantifying phenotypic traits. *J. Complex Networks*, 5:145, 2017.

[31] C. Lopez-Molina, B. de Baets, and H. Bustince. Quantitative error measures for edge detection. *Pattern recognition*, 46:1125–1139, 2013.

[32] C. Lopez-Molina, G. V. D. de Ulzurrun, J. M. Baetens, J. Van den Bulcke, and B. De Baets. Unsupervised ridge detection using second order anisotropic gaussian kernels. *Signal Processing*, 116:55–67, 2015.

[33] S. Marbach, K. Alim, N. Andrew, A. Pringle, and M. P. Brenner. Pruning to increase taylor dispersion in physarum polycephalum networks. *Physical Review Letters*, 117, 2016.

[34] E. Meijering, M. Jacob, J. Sarria, P. Steiner, H. Hirling, and M Unser. Design and validation of a tool for neurite tracing and analysis in fluorescence microscopy images. *Cytometry*, 58A:167176, 2004.

[35] F. Meyer. Topographic distance and watershed lines. *Signal Processing*, 38:113125, 1994.

[36] Y. Mileyko, H. Edelsbrunner, C.A. Price, and J.S. Weitz. Hierarchical ordering of reticular networks. *PLoS One*, 7:e36715, 2012.

[37] M.C. Morrone and R.A. Owens. Feature detection from local energy. *Pattern Recognition Letters*, 6:303 – 313, 1987.

[38] C.D. Murray. The physiological principle of minimum work applied to the branching of arteries. *J. Gen. Physiol.*, 9:835–841, 1926.

[39] B. Obara, V. Grau, and M. D. Fricker. A bioimage informatics approach to automatically extract complex fungal networks. *Bioinformatics*, 28:2374–81, 2012.

[40] J.-P. Onnela, D.J. Fenn, M.A. Reid, S.and Porter, P.J. Mucha, M.D. Fricker, and N.S. Jones. Taxonomies of networks from community structure. *Phys. Rev. E*, 86: 036104, 2012.

[41] C. R. Reid and M. Beekman. Solving the towers of hanoi - how an amoeboid organism efficiently constructs transport networks. *J. Exp. Biol.*, 216:1546–1551, 2013.

[42] C. R. Reid, T. Latty, A. Dussutour, and M. Beekman. Slime mold uses an externalized spatial "memory" to navigate in complex environments. *PNAS*, 109:17490–17494, 2012.

[43] C. R. Reid, H. MacDonald, R. P. Mann, J. A. R. Marshall, T. Latty, and S. Garnier. Decision-making without a brain: how an amoeboid organism solves the two-armed bandit. *Journal of the Royal Society Interface*, 13, 2016.

[44] T. Saigusa, A. Tero, T. Nakagaki, and Y. Kuramoto. Amoebae anticipate periodic events. *Physical Review Letters*, 1, 2008.

[45] T. Saito and M. Rehmsmeier. The precision-recall plot is more informative than the roc plot when evaluating binary classifiers on imbalanced datasets. *PLOS One*, 10:e0118432, 2015.

[46] T.F. Sherman. On connecting large vessels to small: The meaning of murray's law. *J. Gen Physiol.*, 78:431–453, 1981.

[47] P.-L. Shui and W.-C. Zhang. Noise-robust edge detector combining isotropic and anisotropic gaussian kernels. *Pattern Recognition*, 45:806 – 820, 2012.

[48] P. Soille. *Morphological Image Analysis: Principles and Applications.* Springer-Verlag, 1999.

[49] C. Steger. An unbiased detector of curvilinear structures. *IEEE Trans. Pattern Analysis and Machine Intelligence*, 20:113–125, 1998.

[50] A. Tero, T. Nakagaki, K. Toyabe, K. Yumiki, and R. Kobayashi. A method inspired by physarum for solving the steiner problem. *International Journal of Unconventional Computing*, 6:109–123, 2010.

[51] A. Tero, S. Takagi, T. Saigusa, K. Ito, D. P. Bebber, M. D. Fricker, K. Yumiki, R. Kobayashi, and T. Nakagaki. Rules for biologically inspired adaptive network design. *Science*, 327:439–442, 2010.

[52] S. Venkatesh and R. Owens. On the classification of image features. *Pattern Recognition Letters*, 11:339–349, 1990.